Post-mortem changes of anisotropic mechanical properties in the porcine brain assessed by MR elastography

Shuaihu Wang[a], **Kevin N. Eckstein**[a], **Charlotte A. Guertler**[a], **Curtis L. Johnson**[b], **Ruth J. Okamoto**[a], **Matthew D.J. McGarry**[c], **Philip V. Bayly**[a,d,*]

[a]Washington University in St. Louis, Mechanical Engineering and Material Science, United States

[b]University of Delaware, Biomedical Engineering, United States

[c]Dartmouth College, Thayer School of Engineering, United States

[d]Washington University in St. Louis, Biomedical Engineering, United States

Abstract

Knowledge of the mechanical properties of brain tissue *in vivo* is essential to understanding the mechanisms underlying traumatic brain injury (TBI) and to creating accurate computational models of TBI and neurosurgical simulation. Brain white matter, which is composed of aligned, myelinated, axonal fibers, is structurally anisotropic. White matter *in vivo* also exhibits mechanical anisotropy, as measured by magnetic resonance elastography (MRE), but measurements of anisotropy obtained by mechanical testing of white matter *ex vivo* have been inconsistent. The minipig has a gyrencephalic brain with similar white matter and gray matter proportions to humans and therefore provides a relevant model for human brain mechanics. In this study, we compare estimates of anisotropic mechanical properties of the minipig brain obtained by identical, non-invasive methods in the live (*in vivo*) and dead animals *(in situ)*. To do so, we combine wave displacement fields from MRE and fiber directions derived from diffusion tensor imaging (DTI) with a finite element-based, transversely-isotropic nonlinear inversion (TI-NLI)

algorithm. Maps of anisotropic mechanical properties in the minipig brain were generated for each animal alive and at specific times post-mortem. These maps show that white matter is stiffer, more dissipative, and more anisotropic than gray matter when the minipig is alive, but that these differences largely disappear post-mortem, with the exception of tensile anisotropy. Overall, brain tissue becomes stiffer, less dissipative, and less mechanically anisotropic post-mortem. These findings emphasize the importance of testing brain tissue properties *in vivo*.

Statement of Significance: In this study, MRE and DTI in the minipig were combined to estimate, for the first time, anisotropic mechanical properties in the living brain and in the same brain after death. Significant differences were observed in the anisotropic behavior of brain tissue post-mortem. These results demonstrate the importance of measuring brain tissue properties *in vivo* as well as *ex vivo,* and provide new quantitative data for the development of computational models of brain biomechanics.

Keywords

Magnetic resonance elastography; Diffusion tensor imaging; Brain tissue stiffness; Anisotropy; Post-mortem changes

1. Introduction

Traumatic brain injury (TBI) is a leading cause of morbidity and mortality [1,2]. TBI is caused by external forces resulting in large linear and angular head accelerations and rapid deformation of the brain tissue [3]. Computational models and simulations can be used to investigate the effects of different loading scenarios and protective interventions [4, 5], and ultimately to improve methods of diagnosis and treatment of TBI [6]. The accuracy of these simulations is strongly dependent on the choice of brain tissue material properties. In particular, knowledge of *in vivo* brain tissue mechanical properties is essential to accurately predicting brain behavior *in vivo*. However, most existing simulations are performed using material properties derived from animal tissue obtained after death [7–10], either excised tissue *in vitro* or intact tissue measured in place (*in situ*) [11–14]. Comparing *in vivo* properties to post-mortem measurements is critical to correctly interpret the mechanical properties of brain tissue measured *ex vivo* and the computational models that have relied on these measurements for the last several decades [15].

The relationship between the mechanical properties of dead brain tissue and those of the intact, living brain remains incompletely characterized [11], despite several landmark studies. Miller et al. [16] performed indentation test on the exposed porcine brain in *vivo* and found brain stiffness on the same order of magnitude as *in vitro* measurements. Bilston [17] has hypothesized that the brain tissue would become softer after death because of the absence of pressurized vasculature. Gefen and Margulies [11] compared indentation testing of the rat brain *in vivo* and *in situ* after removing the skull to access the brain, and found that the living brain tissue was stiffer than the preconditioned tissue *in situ*. Although their conclusions are disparate, these prior studies provided some insights into post-mortem changes in brain tissue properties. These studies were constrained by the limitations of the indentation method. Removing the skull and exposing the brain perturbs the brain's physical and chemical environment. Also, indentation of the intact brain only measures properties

near the surface and is sensitive to adhesion and contact forces between the tissue and the probe.

Magnetic resonance elastography (MRE) provides a non-invasive method for measuring the dynamic deformation of the brain tissue [18], which can then be inverted to estimate the parameters of a viscoelastic material model. Inversion methods to estimate the mechanical properties include local frequency estimation [19], direct inversion of the viscoelastic shear wave equation [20–22], or inverse finite element (FE) methods [23–25]. MRE has been used for the mechanical characterization of biological tissues, including brain, liver, heart, and muscle [26–28], as well as the study of changes in stiffness and viscosity due to aging, disease, and injury [29–31]. A recent study used MRE in a single minipig to measure how brain tissue stiffness *in situ* differs from *in vivo*. In this animal, an immediate brain stiffening of up to 58 % was observed within three minutes post-mortem and a continuing stiffening of up to 142 % was observed within 45 mins [14]. Guertler et al. [32] performed MRE in the intact minipig brain and brain tissue slabs from the same animal embedded in gel at overlapping frequencies. They found that *in vivo* tissue appeared stiffer than *ex vivo* brain tissue samples at frequencies of 100 Hz and 125 Hz, but measurements agreed more closely at lower frequencies. Bertalan et al. [33] used MRE to measure the stiffness change of the mouse brain as the animal dies. They reported an increase in brain stiffness after respiratory arrest even when cardiac function is still preserved, and cerebral stiffness further increases by up to 30 % within 5 mins of cardiac arrest.

Most previous MRE studies, including all prior comparisons of *in vivo* and *ex vivo* properties [32,34], assume that brain tissue is mechanically isotropic. If the tissue is anisotropic, as in fibrous tissue such as white matter (WM) in the brain, the simplifying assumption of anisotropy can lead to uncertainty and increased variability in mechanical property estimates [35]. Several anisotropic MRE inversion methods have been proposed, with different underlying linear viscoelastic material models. For example a nine-parameter model for brain white matter (WM) [36], and a two-parameter model for breast tissue [22,37]. Feng et al. [10] proposed a nearly-incompressible, transversely isotropic material model with three parameters, which has been used to describe the mechanical behavior of anisotropic phantoms and fibrous tissues in MRE [38–40]. The transversely isotropic model is the simplest anisotropic material, having a single axis of symmetry, often aligned with the dominant direction of reinforcing fibers [41]. Anisotropic MRE methods typically assume brain tissue is a fibrous material and use diffusion tensor imaging (DTI) to estimate fiber orientation. DTI is a powerful technique to detect direction-dependent water diffusion in biological tissues at a microstructural level [42], which can then be utilized to explore brain tissue microstructural organization [43]. This fiber direction is assumed to be the direction of maximal diffusivity from DTI and is incorporated into the underlying material model to interpret material anisotropy in terms of the effect of axonal fibers on the mechanical behavior of the brain tissue [24,44].

McGarry et al. [24] incorporated the transversely isotropic linear viscoelastic model [10,45,46] into the nonlinear inversion (NLI) framework to reproduce heterogeneous, anisotropic properties. NLI relies on a computational model of the mechanical motion of heterogeneous tissue and iteratively estimates mechanical properties that best reproduce the

measured displacements [24,25]. Transversely isotropic NLI (TI-NLI) and other anisotropic MRE methods also need sufficient and varied displacement data to ensure the accurate estimation of mechanical parameters [47]. Anderson et al. [35] and Wang et al. [48] proposed multi-excitation MRE with more than one actuator or actuator location to provide sufficiently diverse displacement data for anisotropic inversion, and TI-NLI incorporates these multiple displacement fields to improve anisotropic property estimation. TI-NLI has been shown to recover accurate (within 1.3 % of true values) heterogenous parameter fields using synthetic data in the presence of measurement noise, and repeatable (coefficient of variation < 7.7 % over 10 scans) property estimates for *in vivo* human brain [24].

Still lacking are direct comparisons between anisotropic mechanical properties estimated throughout the brain by the same method, both *in vivo* (alive) and *in situ* (post-mortem). The primary objective of this paper is thus to measure anisotropic mechanical properties in the minipig brain alive and at various times post-mortem, and to characterize changes in tissue behavior. To this end, shear wave displacement fields were obtained by MRE using three different mechanical actuator configurations in juvenile Yucatan minipigs *in vivo* and *in situ*. Structural anisotropy (fiber orientation) was characterized by the diffusion tensors estimated by DTI. Anisotropic mechanical parameters were then estimated by the TI-NLI algorithm using combined MRE and DTI data obtained *in vivo*, then an hour after death, and up to four hours post-mortem.

2.   Methods

In vivo and *in situ* anatomical MRI, DTI, and MRE scans were performed (Siemens Prisma® 3T scanner) on eight Yucatan minipigs (age range: 6–8 months; weight range: 27–46 kg; Supplementary Table ST1). All studies were approved by the Washington University in St. Louis Institutional Animal Care and Use Committee and supervised by veterinary staff.

2.1.   Experimental methods and data acquisition

2.1.1.   In vivo scanning—Animals were anesthetized with Telazol–Ketamine–Xylazine (TKX) intramuscular injection. An IV catheter and endotracheal tube were placed prior to scanning. Anesthesia was maintained continuously with 1–2 % isoflurane via endotracheal tube. Pulse, respiration, and oxygen saturation (SpO_2) were monitored by veterinary staff during the scan. The anesthetized minipigs were positioned in dorsal recumbency on the scanner table with head placed in the bottom half of the Siemens Head/Neck 20 coil (Fig. 1A). A combination of bean-bags and foam padding was used to maintain a stable head position.

T_1-weighted and T_2-weighted anatomical MR images were acquired at the beginning of each scan at 0.8 mm isotropic resolution in an image volume of $205 \times 205 \times 154$ mm^3 (matrix size of 256×256, 192 slices). Two averages were included for each acquisition to improve the signal-to-noise ratio. Total acquisition time for the anatomical image volumes was approximately 21 mins.

DTI was performed to estimate WM fiber direction. Diffusion-weighted images (DWI) were obtained using 30 diffusion-weighted directions and *b*-value of 1000 with two averages and

8 additional $b = 0$ acquisitions and dorsal-ventral (DV) phase-encoding direction. The image volumes were acquired at 1.5 mm isotropic resolution with a matrix size of 128×128 and 48 slices for an image volume of $192 \times 192 \times 72$ mm^3 using a single-shot echo-planar imaging (EPI) acquisition A second set of DWI was acquired with the same image volumes and imaging parameters but with reversed (*i.e.* Ventral–Dorsal) phase encoding direction. Total acquisition time for the DWI was approximately 15 mins.

For MRE, shear waves were induced using a custom multi-directional jaw actuator with three configurations at a frequency of 100 Hz [32,48]. The harmonic motion was transmitted from a pneumatic driver (Resoundant™, Rochester, MN) by plastic tubing to the passive jaw actuator, which consists of two flexible plastic bottles. After positioning the minipig, the custom actuator was inserted and secured in the minipig's mouth with straps. The bottles were pre-loaded against the rear molars to minimize slippage between the teeth and actuator. The three actuator configurations were: (1) both actuator bottles actuated in-phase ("Both" actuation, Fig. 1B); (2) only the left side actuated ("Left" actuation, Fig. 1C); (3) only the right side actuated ("Right" actuation, Fig. 1D).

The images of the harmonic displacement field were acquired with the same 1.5 mm isotropic voxel resolution and center of slice groups as the DTI scan but with a slightly smaller in-plane imaging volume of $180 \times 180 \times 72$ mm^3 (120×120 matrix, 48 slices) using a 2D multishot spiral sequence with OSCILLATE acceleration [49,50]. Multiple sinusoidal motion-encoding cycles of gradient strength 70 mT/m were synchronized with motion to induce phase contrast proportional to displacement (1.498 μm/rad) and collect 8 temporal samples acquired per period of harmonic motion. The repetition time (TR) was 4800 ms and the echo time (TE) was 60 ms. For each actuator configuration, a second set of scans with 2.0 mm isotropic voxels was acquired using an EPI MRE imaging sequence at 100 Hz with a reduced motion encoding gradient strength of 40 mT/m, and these image volumes were used for temporal unwrapping when required [51]. The total time required to obtain MRE data for all three actuator configurations was 30–40 mins.

2.1.2.   In situ scanning—After *in vivo* scanning was completed, the minipig was euthanized by intravenous (IV) injection of sodium pentobarbital; extension lines were used to allow IV injection while the animal is in the scanner without inducing movement between *in vivo* and *in situ* scanning. *In situ* scanning was initiated 5 mins after heartbeat cessation was determined by pulse oximeter, and performed with three different time intervals post-mortem, 60 mins (all 8 animals), 150 mins (4 animals), and 240 mins (3 animals). Since each scan (anatomical, DTI, and MRE) takes several minutes, the post-mortem time interval indicates the average delay between corresponding MRE experiments. The interval between *in vivo* and first *in situ* MRE scanning corresponded to approximately the time needed for euthanasia, anatomical imaging, and diffusion-weighted imaging. Identical imaging volumes and procedures were used for both *in vivo* and *in situ* scanning. In 4 of 8 minipigs, the core temperature of the minipig was estimated by measuring axillary temperature throughout scanning using an MR-compatible gallium arsenide fiber optic thermometer probe (OpSens Medical™, QC, Canada).

2.2.   Image data analysis

2.2.1.   Diffusion tensor imaging—Diffusion-weighted images were corrected for motion and eddy currents with TORTOISE v3.2 [52] and then for EPI distortion using DRBUDDI [53]. The diffusion tensor is estimated at each voxel using nonlinear tensor fitting [54]. Fractional anisotropy (FA) was calculated from the diffusion tensor eigenvalues (λ_1, λ_2, and λ_3),

$$\text{FA} = \sqrt{\frac{3}{2}} \sqrt{\frac{\left(\lambda_1 - \hat{\lambda}\right)^2 + \left(\lambda_2 - \hat{\lambda}\right)^2 + \left(\lambda_3 - \hat{\lambda}\right)^2}{\sqrt{\lambda_1^2 + \lambda_2^2 + \lambda_3^2}}}$$

(1)

where $\hat{\lambda} = (\lambda_1 + \lambda_2 + \lambda_3)/3$, is the mean diffusivity (MD). Fiber direction was assumed to be the direction of maximal diffusivity, or axial diffusivity (AD), which is the first (largest) principal eigenvector of the diffusion tensor. The radial diffusivity (RD), $\lambda_R = (\lambda_2 + \lambda_3)/2$, describes the diffusivity perpendicular to the fiber direction.

2.2.2.   MRE bulk motion and dynamic deformation—Phase-contrast images encoding harmonic displacement for 8 temporal samples were spatially unwrapped using PRELUDE [55] from FMRIB's Software Library (FSL) [56], if required. Displacement field data were fitted into a model of rigid body displacement to estimate the rigid body motion, or bulk motion, of the brain. Then, the dynamic deformation, or wave motion, was calculated by subtracting bulk motion from the total displacement field [57], which was checked for sign and direction consistency for further input to the inversion algorithm (Supplementary Figure S1).

2.2.3.   Transversely isotropic nonlinear inversion (TI-NLI)—The wave motion fields measured by MRE and fiber directions obtained by DTI were processed with TI-NLI to estimate the anisotropic mechanical properties. Subzone-based NLI [25,58] is based on an iterative minimization of an objective function (Φ) for each subzone:

$$\phi(\theta) = \sum_{i=1}^{N_m} \left\{ \left(u_{m(i)} - u_{c(i)}(\theta)\right)\left(u_{m(i)} - u_{c(i)}(\theta)\right)^* \right\},$$

(2)

where $u_{m(i)}$ denotes the complex-valued amplitude of the ith displacement measurement, $u_{c(i)}(\theta)$ are the analogous displacements calculated with the forward computational model based on the current estimate of the properties, θ, N_m is the number of subzones and * represents the complex conjugate [25]. In this work, 16 mm cubic subzones were used, corresponding to roughly 0.75 shear wavelengths per zone for *in vivo* scanning and 0.65 wavelengths per zone for *in situ* scanning, which is in the range for stable estimates in NLI (*i.e.*, the estimated parameters are insensitive to variations in subzone size) [59].

The underlying material model of TI-NLI is the nearly incompressible transversely isotropic (NITI) model with three parameters [10,24]:

1. $G^* = G' + iG''$, the complex shear modulus in the plane of isotropy.

2. $\phi = G'_1/G' - 1$, the relative difference in shear storage modulus for shear in planes perpendicular to the plane of isotropy, G'_1, relative to the in-plane shear modulus, G'.

3. $\zeta = E'_1/E' - 1$, the relative difference in Young's modulus for stretch along the fiber axis, E'_1, relative to Young's modulus for stretch normal to the fiber axis, E'.

The two tensile moduli are related to these three parameters by $E'_1 = G'(4\zeta + 3)$ and $E' = G'(4\zeta + 3)/(\zeta + 1)$ in the limit of incompressibility [45]. The complex shear modulus is then reformulated to baseline shear stiffness $\mu = 2|G^*|^2/(G' + |G^*|)$, which governs the wave speed of harmonic shear waves in the plane of isotropy [19], and damping ratio $\xi = G''/2G'$, which describes the attenuation of harmonic motion in brain tissue [60].

TI-NLI can incorporate displacement data from multiple actuation scenarios to recover a single set of properties, and more displacement fields should provide a greater diversity of shear wave propagation and polarization directions to probe anisotropic effects more thoroughly. Assuming all motion measurements have sufficient SNR and the NITI model is appropriate, the inversion should recover approximately the same properties for any combination of two or more displacement fields. As a check on data consistency, four combinations of displacement fields from three different actuator configurations, BLR, BL, BR, and LR, were used to estimate the material properties. The initials "*B*", "*L*" and "*R*" refer to the displacement field obtained by using "Both," "Left," and "Right" actuator configurations, respectively (Fig. 1). For each inversion, the algorithm uses all the data from the included configurations.

Images were masked prior to NLI by manually segmenting brain regions using ITK-Snap [61] (Fig. 2A and B). The medulla, pons, and olfactory bulbs were then removed prior to the estimation of material parameters, since the size of these regions is relatively small compared to both the approximate wavelengths of shear waves and the subzone size. The resulting brain volume of interest (VOI; Fig. 2C) includes roughly 80 % of the total brain voxels in each scan. Voxels inside this region with both FA greater than 0.2 [62] and with diffusion consistent with a prolate or "linear" diffusion ellipsoid $(\lambda_1 - \lambda_2) > (\lambda_2 - \lambda_3)$ [63] are denoted as WM for data analysis (Fig. 2D), typically ~25 % of the brain VOI. Gray matter (GM) voxels were defined as voxels within the brain VOI with FA < 0.2 (approximately 55 % of the brain VOI). Cerebrospinal fluid (CSF) was automatically segmented and removed from all analyzed regions (brain VOI, GM, and WM) using a threshold that eliminates hyperintense voxels in T_2-weighted images interpolated onto MRE images. Voxels with FA > 0.2 and oblate or "planar" diffusion ellipsoids, $(\lambda_1 - \lambda_2) < (\lambda_2 - \lambda_3)$, are not included in either WM or GM as defined here, since those features suggest tissue has underlying structure but not transverse isotropy.

2.2.4. Statistical analysis—For statistical analysis, mean values of the diffusion parameters FA and MD from DTI and the four mechanical parameters estimated by TI-NLI (using the BLR combined data set) in each brain VOI and in the WM and GM sub-volumes

were treated as individual data points, with means and standard deviations computed over all scans. Results were each analyzed separately for brain VOI, WM sub-volume, and GM sub-volume using one-way analysis of variance (ANOVA) with the time point as a categorical factor, followed by Tukey's test for multiple comparisons of each time point with all other time points, with a mixed model to handle the missing values (GraphPad Prism, San Diego, CA). Then, the four mechanical parameters were each analyzed using mixed model two-way ANOVA with both time point and tissue type (WM/GM) as categorical factors, followed by Sidak's test for multiple comparisons. $p < 0.05$ was considered statistically significant.

3. Results

Fig. 3 shows examples of anatomical structure, fiber direction, and wave motion generated by the "Both" actuator configuration for one axial and one sagittal slice of a representative minipig brain. Displacement components were measured in all three directions: U denotes the component in the right-left (RL) direction; V the component in the dorsal-ventral (DV) direction; and W the component in the rostral-caudal (RC) direction. The maximum displacement amplitude is about 2 μm. The wavelength of shear wave fields from the three *in situ* MRE scans are visibly greater than those of *in vivo* scans, particularly in the W-component (RC direction).

Fig. 4 shows the mean FA and mean MD values calculated from diffusion tensors of all eight animals at different time points. The mean FA value (*in vivo*) was significantly different from the mean FA (60 mins *pm*) ($p < 0.0001$ for brain VOI, $p = 0.0066$ for WM, and $p = 0.0116$ for GM), mean FA (150 mins *pm*) ($p = 0.0007$ for brain VOI, $p = 0.0040$ for WM, and $p < 0.0001$ for GM), and mean FA (240 mins *pm*) ($p < 0.0080$ for brain VOI, $p = 0.0270$ for WM, and $p = 0.0003$ for GM). No statistically significant difference was observed between the mean FA values from the three *in situ* scans, indicating that diffusion anisotropy increases after euthanasia and remains stable with post-mortem time over the next four hours. In contrast, the mean diffusivity decreases after death ($p < 0.0001$, MD, Fig. 4B) and keeps decreasing over 2.5 h post-mortem time, before apparently stabilizing by 4 h post-mortem time.

Fig. 5 displays representative TI-NLI-estimated material properties using the "BLR" input in animal MP6 from both *in vivo* and *in situ* scanning. Estimates of baseline shear stiffness appear noticeably higher after death, which is consistent with the longer wavelength after death seen in Fig. 3C. Estimates of damping ratio, ξ, shear anisotropy, ϕ, and tensile anisotropy, ζ, are generally lower after death, but no clear temporal changes in these parameters were seen with increasing post-mortem time.

The mean values of these four parameters in the entire brain VOI, the WM sub-volume, and the GM sub-volume are depicted in Fig. 6 for each minipig. For the *in vivo* estimates, the mean values of damping ratio, ξ, shear anisotropy, ϕ, and tensile anisotropy, ζ, are markedly higher in WM, and a small but consistent difference in baseline shear stiffness, μ, is seen between WM and GM. The mean values of damping ratio, shear anisotropy, and tensile anisotropy are generally lower after death, but the baseline shear stiffness increases

dramatically after death and becomes stable with post-mortem time. The differences between WM and GM in terms of shear stiffness and damping ratio become smaller after death.

Estimated mechanical parameters in the entire brain VOI from all four scans are shown in Fig. 7, along with the results of statistical analysis. The shear stiffness, μ (*in vivo*), was found to be significantly different from μ (60 mins *pm*) ($p < 0.0001$), μ (150 mins *pm*) ($p < 0.0001$), and μ (240 mins *pm*) ($p < 0.0001$). The damping ratio, ξ, (*in vivo*) was significantly different from ξ (60 mins *pm*) ($p < 0.0001$), ξ (150 mins *pm*) ($p < 0.0001$), and ξ (240 mins *pm*) ($p < 0.0001$). The shear anisotropy, ϕ (*in vivo*) was significantly different from ϕ (60 mins *pm*) ($p = 0.0394$) and ϕ (240 mins *pm*) ($p = 0.0316$), but not ϕ (150 mins *pm*). Differences in tensile anisotropy, ζ, among these four time points are not statistically significant. For all four mechanical parameters, no significant differences were observed between estimates from any of the three *in situ* scans. This suggests that the shear stiffness increases (~50 %) and damping and shear anisotropy decrease (~60 % for ξ, and ~80 % for ϕ) after death, while tensile anisotropy was relatively unchanged between *in vivo* and post-mortem conditions.

Fig. 8 displays the estimated mechanical parameters in WM and GM over all four scan times. Baseline shear stiffness in WM is slightly higher than in GM *in vivo* ($p = 0.0018$) and 60 mins post-mortem ($p = 0.0014$), and the difference between WM and GM decreases when the post-mortem (*pm*) time interval becomes longer ($p = 0.8194$ for 150 mins *pm* and $p = 0.3048$ for 240 mins *pm*). The damping ratio was higher in WM than GM *in vivo* ($p < 0.0001$), but becomes similar in WM and GM after death ($p = 0.9998$ for 60 mins *pm*, $p = 0.9121$ for 150 mins *pm*, and $p = 0.4678$ for 240 mins *pm*). Shear anisotropy is higher in WM than GM *in vivo* ($p = 0.0061$) and 60 mins post-mortem ($p = 0.0004$), and the difference between WM and GM decrease with the post-mortem time ($p = 0.1462$ for 150 mins *pm* and $p = 0.1335$ for 240 mins *pm*). Finally, tensile anisotropy was greater in WM than GM for all four scan times ($p < 0.0001$ for *in vivo*, $p < 0.0001$ for 60 mins *pm*, $p < 0.0001$ for 150 mins *pm*, and $p = 0.0041$ for 240 mins *pm*). Overall, WM appears stiffer, more dissipative, and more anisotropic than GM when the animal is alive, but mechanical differences between WM and GM generally diminish after death. Numerical values of parameter estimates are tabulated in Supplementary Table ST2.

4. Discussion

This study provides the first investigation of post-mortem changes of brain anisotropic mechanical properties by MRE in a large animal model: the minipig. The minipig has a gyrencephalic brain with prominent WM tracts and general anatomical and physiological similarities to the human brain [64]. Because of these features, the mechanical behavior of the porcine brain has frequently been measured to try to understand and predict the response of the human brain to loading [10, 32,34].

Our imaging studies included the characterization of diffusion in the brain by DTI before and after death (Supplementary Figures S2 and S3). A decrease in mean diffusivity (MD) after death was observed and is consistent with existing data [65]. After death, diffusion

measurements were insensitive to post-mortem time up to four hours, which is consistent with prior studies in minipigs [66] and in the human brain [67]. We observed a small but significant post-mortem increase in diffusion anisotropy (FA), which is driven by a slightly larger relative decrease in radial diffusivity compared with axial diffusivity (Supplementary Figure S4). The decrease in MD and increase of FA after death have been speculated to be related to changes in viscosity in the intracellular space, which is likely caused by the breakdown of macromolecular structural proteins, the increased tortuosity in the shrunken extracellular space, and the concomitant restriction of water movement across fibers [68].

The three actuator configurations, "Both", "Left", and "Right", lead to differing motion patterns (required for TI-NLI) but with some common features (Supplementary Figure S5). The magnitudes of wave fields are on the order of 1–2 μm, which are similar to those in human MRE studies performed with a "paddle actuator" [69] and with a "pillow" actuator [57], as well as to those in previous studies in the minipig brain [32,48]. The magnitudes of displacements in the third *in situ* scans are lower, as are the octahedral shear strains (Supplementary Figure S6), likely due to the onset of rigor mortis (post-mortem musculoskeletal stiffening) reducing jaw motion. The wave fields from the three actuator configurations provide four combinations of input to the TI-NLI inversion algorithm, and the estimated mechanical properties with these four combinations exhibit qualitatively and quantitatively similar patterns (Supplementary Figure S7 and Supplementary Table ST3). In a subset of scan time points, isotropic NLI was also performed (Supplementary Table ST4). Consistent with prior studies [48], variations in estimates between different combinations were typically less than 0.1 kPa in shear stiffness, less than 0.02 for damping ratio, and less than 0.05 for shear anisotropy and tensile anisotropy. The agreement between results from different actuator combinations suggests that TI-NLI parameter estimates are robust to details of the excitation.

Estimates of shear stiffness, μ, in the range of 3.8 to 4.5 kPa, and damping ratio, ξ, in the range of 0.1–0.2 were observed in the minipig brain. While damping ratio is similar to prior estimates, the shear stiffness is somewhat higher than our previous estimates of μ from ~3–4 kPa [48] in juvenile minipigs (3–6 months old); this difference in stiffness may be attributable to the trend of increasing stiffness with age observed in the previous study [48]. Accounting for effects of frequency, the current estimates of shear stiffness are consistent with estimates of μ from ~2.6 to 2.8 kPa (WM higher than GM) in human brain at 50 Hz using anisotropic MRE [70], and current estimates of damping are similar to estimates in human brain at 50 Hz using isotropic MRE [71]. In WM, estimates of shear anisotropy (ϕ) are in the range of 0.07–0.20, and tensile anisotropy (ζ) are between 0.3–0.5, which are similar to estimates in human WM [70,72], as well as to our previous estimates in minipigs [48]. The effective image resolution of each parameter is influenced by the shear wavelength, data resolution, data quality, and relative parameter sensitivity which together determine the regularization required to maintain stability of NLI [73]. Preliminary results with realistic simulated data suggest the effective resolution of μ is approximately 5 mm [24], whereas the damping ratio and anisotropy parameters have lower effective resolution of ~10 mm. A comprehensive phantom study would be necessary to determine the experimentally achievable contrast-detail resolution for all anisotropic parameters [74]. We

are currently developing 3D-printed phantoms for this purpose [75] and plan such a study in future work.

For the post-mortem properties, our estimates of shear stiffness are in the range of 5–7 kPa, and damping ratio is in the range of 0.06 to 0.10. Previous studies of the post-mortem mechanical properties of animal brains from *in situ* scanning show differences spanning an order of magnitude in reported properties [11–14,33]. Inter-species variability and testing protocol differences can explain some of these discrepancies, and the post-mortem time interval might be an important factor that may lead to this scatter. In WM, our estimates of shear anisotropy (ϕ) post-mortem are roughly from −0.1 to 0.1, and tensile anisotropy (ζ) post-mortem is between 0 and 0.4.

We observed an increase in shear stiffness and a decrease in damping ratio after death in both WM and GM, consistent with prior studies in porcine brain [12] and mouse brain [13,33]. Shear anisotropy decreases post-mortem, though tensile anisotropy apparently does not. These trends might be related to cytotoxic edema following euthanasia by barbiturate overdose. Complete depolarization of cell membranes occurs after death [76], and the collapse of ionic homeostasis leads to a substantial influx of water, which will result in neuronal and astroglial swelling [77]. Associated with the enhanced influx of glymphatic cerebral spinal fluid and suppressed efflux of interstitial fluid from the cranium, cerebral edema leads to a noticeable increase in intracranial pressure [78] and tissue stiffening [13]. The decrease in brain tissue damping could possibly be related to neuronal cell swelling, which leads to shrinkage of extracellular space and restricts extracellular water movement [68]. The shrinkage of extracellular space may also lead to structural changes of the extra-axonal matrix and affect the fiber-matrix interactions that underlie shear anisotropy. Additionally, the loss of perfusion after death is another significant factor that impacts brain mechanical properties [17,79–81], both directly and indirectly. While lower perfusion has been associated with decreased stiffness of brain tissue *in vivo*, the total cessation of cerebral blood flow leads to a lack of oxygen and nutrients, resulting in cell damage or death. This degrades the integrity of the cellular structure and extracellular matrix [82] and may trigger the changes in fluid distribution noted above. The post-mortem breakdown of intracellular proteins and cytoskeletal organization in WM appears to affect shear anisotropy more than tensile anisotropy [83]. The structure of axons themselves apparently does not break down completely in this early post-mortem interval [83], as evidenced by the stability of tensile anisotropy. *In vivo*, the differences between WM and GM are related to their cytoarchitecture and matrix properties [84,85]. After death, the breakdown of cellular structure and extracellular matrix, as well as edema, likely reduces the microstructural differences between WM and GM.

Although mean diffusivity and stiffness may change with temperature [86,87], observed temperature changes in this study were relatively low (about −1 °C per hour following death) (Supplementary Table ST1). Therefore, we did not expect temperature change to affect immediate post-mortem measures, while 150 mins and 240 mins post-mortem measures may have been slightly affected.

We acknowledge several limitations of this study. First, compared to the human brain, the minipig brain is small ($< 110\ cm^3$) so that, relative to brain anatomical structure, images are acquired at a lower effective resolution in the minipig than in humans despite the use of state-of-the-art imaging sequences and instrumentation. Another limitation of this study is that MRE was performed at only one frequency (100 Hz), even though the mechanical response of soft tissue depends on frequency. In the future, new inversion methods and accelerated sequences will allow us to incorporate data from multiple frequencies, which will enable us to explore frequency-dependent behavior in the anisotropic mechanical properties. The NITI model used in this study only captures material behavior with a single dominant fiber direction, so that parameter estimates will be difficult to interpret in regions with crossing fibers, as in some regions of brain WM. In the current study, such regions were assumed to correspond to voxels with "planar" diffusion ellipsoids, which were excluded from both the GM and WM regions analyzed. Ongoing work is aimed at incorporating material models into NLI to describe tissue with two fiber families [88]. An isotropic damping ratio was assumed in the current study [89]; ongoing work will allow us to investigate the possibility of anisotropic damping in the future. Finally, while the current data (from one *in vivo* and three *in situ* scans at different post-mortem times) describe how brain tissue mechanical properties change with time, further work is needed to elucidate the underlying biological and biochemical processes underlying these mechanical changes.

5. Conclusion

This study is the first to investigate post-mortem changes in anisotropic mechanical properties of brain tissue in a large animal model. MRE data were collected using a multi-excitation method to produce diverse shear wave fields in the minipig brain. Fiber directions are estimated from DTI and combined with MRE data for the estimation of anisotropic mechanical properties estimation by TI-NLI inverse finite element method. When the minipig is alive, WM is more anisotropic than GM, both structurally and mechanically, as well as stiffer and more dissipative. The differences between WM and GM diminish post-mortem, except for tensile anisotropy. Overall, brain tissues become more anisotropic in diffusion, but stiffer, less damped, and less mechanically-anisotropic after death. These notable differences between the anisotropic mechanical properties of living and dead brain tissue have important consequences for understanding and predicting the response of the brain in injury, neurosurgery, and development.

Supplementary Material

Refer to Web version on PubMed Central for supplementary material.

Acknowledgment

Data availability

Data will be made available on request.

References

[1]. Najem D, Rennie K, Ribecco-Lutkiewicz M, Ly D, Haukenfrers J, Liu Q, Nzau M, Fraser DD, Bani-Yaghoub M, Traumatic brain injury: classification, models, and markers, Biochem. Cell Biol 96 (2018) 391–406, 10.1139/bcb-2016-0160. [PubMed: 29370536]

[2]. Rutland-Brown W, Langlois JA, Thomas KE, Xi YL, Incidence of traumatic brain injury in the United States, 2003, J. Head Trauma Rehabil 21 (2006) 544. [PubMed: 17122685]

[3]. Lota KS, Malliaropoulos N, Blach W, Kamitani T, Ikumi A, Korakakis V, Maffulli N, Rotational head acceleration and traumatic brain injury in combat sports: a systematic review, Br. Med. Bull 141 (2022) 33–46, 10.1093/bmb/ldac002. [PubMed: 35107134]

[4]. Panzer MB, Myers BS, Capehart BP, Bass CR, Development of a finite element model for blast brain injury and the effects of CSF cavitation, Ann. Biomed. Eng 40 (2012) 1530–1544, 10.1007/s10439-012-0519-2. [PubMed: 22298329]

[5]. Liu Y, Lu Y, Shao Y, Wu Y, He J, Wu C, Mechanism of the traumatic brain injury induced by blast wave using the energy assessment method, Med. Eng. Phys 101 (2022) 103767, 10.1016/j.medengphy.2022.103767. [PubMed: 35232553]

[6]. Zhao W, Ji S, White matter anisotropy for impact simulation and response sampling in traumatic brain injury, J. Neurotrauma 36 (2019) 250–263, 10.1089/neu.2018.5634. [PubMed: 29681212]

[7]. Franze K, Janmey PA, Guck J, Mechanics in neuronal development and repair, Annu. Rev. Biomed. Eng 15 (2013) 227–251, 10.1146/annurev-bioeng-071811-150045. [PubMed: 23642242]

[8]. Forte AE, Gentleman SM, Dini D, On the characterization of the heterogeneous mechanical response of human brain tissue, Biomech. Model. Mechanobiol 16 (2017) 907–920, 10.1007/s10237-016-0860-8. [PubMed: 27933417]

[9]. Budday S, Sommer G, Haybaeck J, Steinmann P, Holzapfel GA, Kuhl E, Rheological characterization of human brain tissue, Acta Biomater. 60 (2017) 315–329, 10.1016/j.actbio.2017.06.024. [PubMed: 28658600]

[10]. Feng Y, Okamoto RJ, Namani R, Genin GM, Bayly PV, Measurements of mechanical anisotropy in brain tissue and implications for transversely isotropic material models of white matter, J. Mech. Behav. Biomed. Mater 23 (2013) 117–132, 10.1016/j.jmbbm.2013.04.007. [PubMed: 23680651]

[11]. Gefen A, Margulies SS, Are in vivo and in situ brain tissues mechanically similar? J. Biomech 37 (2004) 1339–1352, 10.1016/j.jbiomech.2003.12.032. [PubMed: 15275841]

[12]. Prevost TP, Jin G, de Moya MA, Alam HB, Suresh S, Socrate S, Dynamic mechanical response of brain tissue in indentation in vivo, in situ and in vitro, Acta Biomater. 7 (2011) 4090–4101, 10.1016/j.actbio.2011.06.032. [PubMed: 21742064]

[13]. Vappou J, Breton E, Choquet P, Willinger R, Constantinesco A, Assessment of in vivo and post-mortem mechanical behavior of brain tissue using magnetic resonance elastography, J. Biomech 41 (2008) 2954–2959, 10.1016/j.jbiomech.2008.07.034. [PubMed: 18805534]

[14]. Weickenmeier J, Kurt M, Ozkaya E, de Rooij R, Ovaert TC, Ehman RL, Butts Pauly K, Kuhl E, Brain stiffens post mortem, J. Mech. Behav. Biomed. Mater 84 (2018) 88–98, 10.1016/j.jmbbm.2018.04.009. [PubMed: 29754046]

[15]. Chatelin S, Constantinesco A, Willinger R, Fifty years of brain tissue mechanical testing: from in vitro to in vivo investigations, Biorheology 47 (2010) 255–276, 10.3233/BIR-2010-0576. [PubMed: 21403381]

[16]. Miller K, Chinzei K, Orssengo G, Bednarz P, Mechanical properties of brain tissue in-vivo: experiment and computer simulation, J. Biomech 33 (2000) 1369–1376, 10.1016/S0021-9290(00)00120-2. [PubMed: 10940395]

[17]. Bilston LE, The effect of perfusion on soft tissue mechanical properties: a computational model, Comput. Methods Biomech. Biomed. Eng 5 (2002) 283–290, 10.1080/10255840290032658.

[18]. Muthupillai R, Lomas DJ, Greenleaf JF, Manduca A, Ehman RL, Magnetic resonance elastography by direct visualization of propagating acoustic strain waves, Science 269 (1995) 1854–1857, 10.1126/science.7569924. [PubMed: 7569924]

[19]. Manduca A, Oliphant TE, Dresner MA, Mahowald JL, Kruse SA, Amromin E, Felmlee JP, Greenleaf JF, Ehman RL, Magnetic resonance elastography: non-invasive mapping of tissue elasticity, Med. Image Anal 5 (2001) 237–254, 10.1016/s1361-8415(00)00039-6. [PubMed: 11731304]

[20]. Okamoto RJ, Clayton EH, Bayly PV, Viscoelastic properties of soft gels: comparison of magnetic resonance elastography and dynamic shear testing in the shear wave regime, Phys. Med. Biol 56 (2011) 6379, 10.1088/0031-9155/56/19/014. [PubMed: 21908903]

[21]. Oliphant TE, Manduca A, Ehman RL, Greenleaf JF, Complex-valued stiffness reconstruction for magnetic resonance elastography by algebraic inversion of the differential equation, Magn. Reson. Med 45 (2001) 299–310, 10.1002/1522-2594(200102)45:2<299::AID-MRM1039>3.0.CO;2-O. [PubMed: 11180438]

[22]. Sinkus R, Tanter M, Catheline S, Lorenzen J, Kuhl C, Sondermann E, Fink M, Imaging anisotropic and viscous properties of breast tissue by magnetic resonance-elastography, Magn. Reson. Med 53 (2005) 372–387, 10.1002/mrm.20355. [PubMed: 15678538]

[23]. Fovargue D, Kozerke S, Sinkus R, Nordsletten D, Robust MR elastography stiffness quantification using a localized divergence free finite element reconstruction, Med. Image Anal 44 (2018) 126–142, 10.1016/j.media.2017.12.005. [PubMed: 29247876]

[24]. McGarry M, Van Houten E, Sowinski D, Jyoti D, Smith DR, Caban-Rivera DA, McIlvain G, Bayly P, Johnson CL, Weaver J, Paulsen K, Mapping heterogenous anisotropic tissue mechanical properties with transverse isotropic nonlinear inversion MR elastography, Med. Image Anal 78 (2022) 102432, 10.1016/j.media.2022.102432. [PubMed: 35358836]

[25]. Van Houten EE, Miga MI, Weaver JB, Kennedy FE, Paulsen KD, Three-dimensional subzone-based reconstruction algorithm for MR elastography, Magn. Reson. Med 45 (2001) 827–837, 10.1002/mrm.1111. [PubMed: 11323809]

[26]. Klatt D, Hamhaber U, Asbach P, Braun J, Sack I, Noninvasive assessment of the rheological behavior of human organs using multifrequency MR elastography: a study of brain and liver viscoelasticity, Phys. Med. Biol 52 (2007) 7281, 10.1088/0031-9155/52/24/006. [PubMed: 18065839]

[27]. Sack I, Rump J, Elgeti T, Samani A, Braun J, MR elastography of the human heart: noninvasive assessment of myocardial elasticity changes by shear wave amplitude variations, Magn. Reson. Med 61 (2009) 668–677, 10.1002/mrm.21878. [PubMed: 19097236]

[28]. Kennedy P, Barnhill E, Gray C, Brown C, van Beek EJR, Roberts N, Greig CA, Magnetic resonance elastography (MRE) shows significant reduction of thigh muscle stiffness in healthy older adults, GeroScience 42 (2020) 311–321, 10.1007/s11357-019-00147-2. [PubMed: 31865527]

[29]. Hiscox LV, Johnson CL, McGarry MDJ, Marshall H, Ritchie CW, van Beek EJR, Roberts N, Starr JM, Mechanical property alterations across the cerebral cortex due to Alzheimer's disease, Brain Commun. 2 (2020) fcz049, 10.1093/braincomms/fcz049.

[30]. Hiscox LV, Johnson CL, McGarry MDJ, Perrins M, Littlejohn A, van Beek EJR, Roberts N, Starr JM, High-resolution magnetic resonance elastography reveals differences in subcortical gray matter viscoelasticity between young and healthy older adults, Neurobiol. Aging 65 (2018) 158–167, 10.1016/j.neurobiolaging.2018.01.010. [PubMed: 29494862]

[31]. Sack I, Beierbach B, Wuerfel J, Klatt D, Hamhaber U, Papazoglou S, Martus P, Braun J, The impact of aging and gender on brain viscoelasticity, Neuroimage 46 (2009) 652–657, 10.1016/j.neuroimage.2009.02.040. [PubMed: 19281851]

[32]. Guertler CA, Okamoto RJ, Schmidt JL, Badachhape AA, Johnson CL, Bayly PV, Mechanical properties of porcine brain tissue in vivo and ex vivo estimated by MR elastography, J. Biomech 69 (2018) 10–18, 10.1016/j.jbiomech.2018.01.016. [PubMed: 29395225]

[33]. Bertalan G, Klein C, Schreyer S, Steiner B, Kreft B, Tzschätzsch H, de Schellenberger AA, Nieminen-Kelhä M, Braun J, Guo J, Sack I, Biomechanical properties of the hypoxic and dying brain quantified by magnetic resonance elastography, Acta Biomater. 101 (2020) 395–402, 10.1016/j.actbio.2019.11.011. [PubMed: 31726251]

[34]. Weickenmeier J, de Rooij R, Budday S, Steinmann P, Ovaert TC, Kuhl E, Brain stiffness increases with myelin content, Acta Biomater. 42 (2016) 265–272, 10.1016/j.actbio.2016.07.040. [PubMed: 27475531]

[35]. Anderson AT, Van Houten EEW, McGarry MDJ, Paulsen KD, Holtrop JL, Sutton BP, Georgiadis JG, Johnson CL, Observation of direction-dependent mechanical properties in the human brain with multi-excitation MR elastography, J. Mech. Behav. Biomed. Mater 59 (2016) 538–546, 10.1016/j.jmbbm.2016.03.005. [PubMed: 27032311]

[36]. Romano A, Scheel M, Hirsch S, Braun J, Sack I, In vivo waveguide elastography of white matter tracts in the human brain, Magn. Reson. Med 68 (2012) 1410–1422, 10.1002/mrm.24141. [PubMed: 22252792]

[37]. Green MA, Geng G, Qin E, Sinkus R, Gandevia SC, Bilston LE, Measuring anisotropic muscle stiffness properties using elastography, NMR Biomed. 26 (2013) 1387–1394, 10.1002/nbm.2964. [PubMed: 23640745]

[38]. Guertler CA, Okamoto RJ, Ireland JA, Pacia CP, Garbow JR, Chen H, Bayly PV, Estimation of anisotropic material properties of soft tissue by MRI of ultrasound-induced shear waves, J. Biomech. Eng 142 (2020), 10.1115/1.4046127.

[39]. Guidetti M, Zampini MA, Jiang Y, Gambacorta C, Smejkal JP, Crutison J, Pan Y, Klatt D, Royston TJ, Axially- and torsionally-polarized radially converging shear wave MRE in an anisotropic phantom made via embedded direct ink writing, J. Mech. Behav. Biomed. Mater 119 (2021) 104483, 10.1016/j.jmbbm.2021.104483. [PubMed: 33838445]

[40]. Hou Z, Guertler CA, Okamoto RJ, Chen H, Garbow JR, Kamilov US, Bayly PV, Estimation of the mechanical properties of a transversely isotropic material from shear wave fields via artificial neural networks, J. Mech. Behav. Biomed. Mater 126 (2022) 105046, 10.1016/j.jmbbm.2021.105046. [PubMed: 34953435]

[41]. Spencer AJM, Continuum Theory of the Mechanics of Fibre-Reinforced Composites, Springer, Vienna, 2014.

[42]. Basser PJ, Pierpaoli C, Microstructural and physiological features of tissues elucidated by quantitative-diffusion-tensor MRI, J. Magn. Reson. B 111 (1996) 209–219, 10.1006/jmrb.1996.0086. [PubMed: 8661285]

[43]. Faria AV, Zhang J, Oishi K, Li X, Jiang H, Akhter K, Hermoye L, Lee S-K, Hoon A, Stashinko E, Miller MI, van Zijl PCM, Mori S, Atlas-based analysis of neurodevelopment from infancy to adulthood using diffusion tensor imaging and applications for automated abnormality detection, Neuroimage 52 (2010) 415–428, 10.1016/j.neuroimage.2010.04.238. [PubMed: 20420929]

[44]. Giordano C, Zappalà S, Kleiven S, Anisotropic finite element models for brain injury prediction: the sensitivity of axonal strain to white matter tract inter-subject variability, Biomech. Model. Mechanobiol 16 (2017) 1269–1293, 10.1007/s10237-017-0887-5. [PubMed: 28233136]

[45]. Tweten DJ, Okamoto RJ, Schmidt JL, Garbow JR, Bayly PV, Estimation of material parameters from slow and fast shear waves in an incompressible, transversely isotropic material, J. Biomech 48 (2015) 4002–4009, 10.1016/j.jbiomech.2015.09.009. [PubMed: 26476762]

[46]. Schmidt JL, Tweten DJ, Benegal AN, Walker CH, Portnoi TE, Okamoto RJ, Garbow JR, Bayly PV, Magnetic resonance elastography of slow and fast shear waves illuminates differences in shear and tensile moduli in anisotropic tissue, J. Biomech 49 (2016) 1042–1049, 10.1016/j.jbiomech.2016.02.018. [PubMed: 26920505]

[47]. Tweten D.j., Okamoto R.j., Bayly P.v., Requirements for accurate estimation of anisotropic material parameters by magnetic resonance elastography: a computational study, Magn. Reson. Med 78 (2017) 2360–2372, 10.1002/mrm.26600. [PubMed: 28097687]

[48]. Wang S, Guertler CA, Okamoto RJ, Johnson CL, McGarry MDJ, Bayly PV, Mechanical stiffness and anisotropy measured by MRE during brain development in the minipig, Neuroimage 277 (2023) 120234, 10.1016/j.neuroimage.2023.120234. [PubMed: 37369255]

[49]. Johnson CL, McGarry MDJ, Van Houten EEW, Weaver JB, Paulsen KD, Sutton BP, Georgiadis JG, Magnetic resonance elastography of the brain using multishot spiral readouts with self-navigated motion correction, Magn. Reson. Med 70 (2013) 404–412, 10.1002/mrm.24473. [PubMed: 23001771]

[50]. McIlvain G, Cerjanic AM, Christodoulou AG, McGarry MDJ, Johnson CL, OSCILLATE: a low-rank approach for accelerated magnetic resonance elastography, Magn. Reson. Med 88 (2022) 1659–1672, 10.1002/mrm.29308. [PubMed: 35649188]

[51]. Kailash KA, Guertler CA, Johnson CL, Okamoto RJ, Bayly PV, Measurement of relative motion of the brain and skull in the mini-pig in-vivo, J. Biomech 156 (2023) 111676, 10.1016/j.jbiomech.2023.111676. [PubMed: 37329640]

[52]. Pierpaoli C, Walker L, Irfanoglu MO, Barnett Al, Basser P, Chang L-C, Koay CG, Pajevic S, Rohde G, Sarlls J, Wu M, TORTOISE: An Integrated Software Package For Processing of Diffusion MRI Data, in: Stockholm, Sweden, 2010. https://archive.ismrm.org/2010/1597.html.

[53]. Irfanoglu MO, Modi P, Nayak A, Hutchinson EB, Sarlls J, Pierpaoli C, DRBUDDI (Diffeomorphic registration for blip-up blip-down diffusion imaging) method for correcting echo planar imaging distortions, Neuroimage 106 (2015) 284–299, 10.1016/j.neuroimage.2014.11.042. [PubMed: 25433212]

[54]. Basser PJ, Mattiello J, LeBihan D, MR diffusion tensor spectroscopy and imaging, Biophys. J 66 (1994) 259–267, 10.1016/S0006-3495(94)80775-1. [PubMed: 8130344]

[55]. Smith SM, Jenkinson M, Woolrich MW, Beckmann CF, Behrens TEJ, Johansen-Berg H, Bannister PR, De Luca M, Drobnjak I, Flitney DE, Niazy RK, Saunders J, Vickers J, Zhang Y, De Stefano N, Brady JM, Matthews PM, Advances in functional and structural MR image analysis and implementation as FSL, Neuroimage 23 (Suppl 1) (2004) S208–S219, 10.1016/j.neuroimage.2004.07.051. [PubMed: 15501092]

[56]. Jenkinson M, Fast, automated, N-dimensional phase-unwrapping algorithm, Magn. Reson. Med 49 (2003) 193–197, 10.1002/mrm.10354. [PubMed: 12509838]

[57]. Badachhape AA, Okamoto RJ, Durham RS, Efron BD, Nadell SJ, Johnson CL, Bayly PV, The relationship of three-dimensional human skull motion to brain tissue deformation in magnetic resonance elastography studies, J. Biomech. Eng 139 (2017), 10.1115/1.4036146.

[58]. Van Houten EE, Paulsen KD, Miga MI, Kennedy FE, Weaver JB, An overlapping subzone technique for MR-based elastic property reconstruction, Magn. Reson. Med 42 (1999) 779–786, 10.1002/(sici)1522-2594(199910)42:4<779::aid-mrm21>3.0.co;2-z. [PubMed: 10502768]

[59]. Anderson AT, Johnson CL, McGarry MDJ, Paulsen KD, Sutton BP, Van Houten EEW, Georgiadis JG, Inversion Parameters based On Convergence and Error Metrics For Nonlinear Inversion MR Elastography, in: Honolulu, HI, USA, 2017. https://archive.ismrm.org/2017/1139.html.

[60]. McGarry MDJ, Van Houten EEW, Use of a Rayleigh damping model in elastography, Med. Biol. Eng. Comput 46 (2008) 759–766, 10.1007/s11517-008-0356-5. [PubMed: 18521645]

[61]. Yushkevich PA, Piven J, Hazlett HC, Smith RG, Ho S, Gee JC, Gerig G, Userguided 3D active contour segmentation of anatomical structures: significantly improved efficiency and reliability, Neuroimage 31 (2006) 1116–1128, 10.1016/j.neuroimage.2006.01.015. [PubMed: 16545965]

[62]. Fil JE, Joung S, Zimmerman BJ, Sutton BP, Dilger RN, High-resolution magnetic resonance imaging-based atlases for the young and adolescent domesticated pig (Sus scrofa), J. Neurosci. Methods 354 (2021) 109107, 10.1016/j.jneumeth.2021.109107. [PubMed: 33675840]

[63]. Westin C-F, Maier SE, Mamata H, Nabavi A, Jolesz FA, Kikinis R, Processing and visualization for diffusion tensor MRI, Med. Image Anal 6 (2002) 93–108, 10.1016/S1361-8415(02)00053-1. [PubMed: 12044998]

[64]. Schomberg DT, Tellez A, Meudt JJ, Brady DA, Dillon KN, Arowolo FK, Wicks J, Rousselle SD, Shanmuganayagam D, Miniature swine for preclinical modeling of complexities of human disease for translational scientific discovery and accelerated development of therapies and medical devices, Toxicol. Pathol 44 (2016) 299–314, 10.1177/0192623315618292. [PubMed: 26839324]

[65]. Scheurer E, Lovblad K-O, Kreis R, Maier SE, Boesch C, Dirnhofer R, Yen K, Forensic application of postmortem diffusion-weighted and diffusion tensor MR imaging of the human brain in situ, Am. J. Neuroradiol 32 (2011) 1518–1524, 10.3174/ajnr.A2508. [PubMed: 21659482]

[66]. Widjaja E, Wei X, Vidarsson L, Moineddin R, Macgowan CK, Nilsson D, Alteration of diffusion tensor parameters in postmortem brain, Magn. Reson. Imaging 27 (2009) 865–870, 10.1016/j.mri.2008.11.009. [PubMed: 19152773]

[67]. Boon BDC, Pouwels PJW, Jonkman LE, Keijzer MJ, Preziosa P, van de Berg WDJ, Geurts JJG, Scheltens P, Barkhof F, Rozemuller AJM, Bouwman FH, Steenwijk MD, Can post-mortem

MRI be used as a proxy for in vivo? A case study, Brain Commun. 1 (2019) fcz030, 10.1093/braincomms/fcz030.

[68]. Ozsunar Y, Grant PE, Huisman TAGM, Schaefer PW, Wu O, Sorensen AG, Koroshetz WJ, Gonzalez RG, Evolution of water diffusion and anisotropy in hyperacute stroke: significant correlation between fractional anisotropy and T2, AJNR Am. J. Neuroradiol 25 (2004) 699–705. [PubMed: 15140707]

[69]. Clayton EH, Genin GM, Bayly PV, Transmission, attenuation and reflection of shear waves in the human brain, J. R. Soc. Interface 9 (2012) 2899–2910, 10.1098/rsif.2012.0325. [PubMed: 22675163]

[70]. Smith DR, Caban-Rivera DA, McGarry MDJ, Williams LT, McIlvain G, Okamoto RJ, Van Houten EEW, Bayly PV, Paulsen KD, Johnson CL, Anisotropic mechanical properties in the healthy human brain estimated with multi-excitation transversely isotropic MR elastography, Brain Multiphys. 3 (2022) 100051, 10.1016/j.brain.2022.100051. [PubMed: 36340644]

[71]. McIlvain G, Schwarb H, Cohen NJ, Telzer EH, Johnson CL, Mechanical properties of the in vivo adolescent human brain, Dev. Cogn. Neurosci 34 (2018) 27–33, 10.1016/j.dcn.2018.06.001. [PubMed: 29906788]

[72]. Smith DR, Guertler CA, Okamoto RJ, Romano AJ, Bayly PV, Johnson CL, Multi-excitation magnetic resonance elastography of the brain: wave propagation in anisotropic white matter, J. Biomech. Eng 142 (2020), 10.1115/1.4046199.

[73]. Jyoti D, McGarry M, Houten EV, Sowinski D, Bayly PV, Johnson CL, Paulsen K, Quantifying stability of parameter estimates for in vivo nearly incompressible transversely-isotropic brain MR elastography, Biomed. Phys. Eng. Express 8 (2022) 035015, 10.1088/2057-1976/ac5ebe.

[74]. Solamen LM, McGarry MD, Tan L, Weaver JB, Paulsen KD, Phantom evaluations of nonlinear inversion MR elastography, Phys. Med. Biol 63 (2018) 145021, 10.1088/1361-6560/aacb08. [PubMed: 29877194]

[75]. Yoon D, Ruding M, Guertler CA, Okamoto RJ, Bayly PV, Design and characterization of 3-D printed hydrogel lattices with anisotropic mechanical properties, J. Mech. Behav. Biomed. Mater 138 (2023) 105652, 10.1016/j.jmbbm.2023.105652. [PubMed: 36610282]

[76]. Santos E, Schöll M,Sánchez-Porras R, Dahlem MA, Silos H, Unterberg A, Dickhaus H, Sakowitz OW, Radial, spiral and reverberating waves of spreading depolarization occur in the gyrencephalic brain, Neuroimage 99 (2014) 244–255, 10.1016/j.neuroimage.2014.05.021. [PubMed: 24852458]

[77]. Risher WC, Croom D, Kirov SA, Persistent astroglial swelling accompanies rapid reversible dendritic injury during stroke-induced spreading depolarizations, Glia 60 (2012) 1709–1720, 10.1002/glia.22390. [PubMed: 22821441]

[78]. Thrane AS, Rangroo Thrane V, Nedergaard M, Drowning stars: reassessing the role of astrocytes in brain edema, Trends Neurosci. 37 (2014) 620–628, 10.1016/j.tins.2014.08.010. [PubMed: 25236348]

[79]. Hetzer S, Birr P, Fehlner A, Hirsch S, Dittmann F, Barnhill E, Braun J, Sack I, Perfusion alters stiffness of deep gray matter, J. Cereb. Blood Flow Metab 38 (2018) 116–125, 10.1177/0271678X17691530. [PubMed: 28151092]

[80]. Chatelin S, Humbert-Claude M, Garteiser P, Ricobaraza A, Vilgrain V, Van Beers BE, Sinkus R, Lenkei Z, Cannabinoid receptor activation in the juvenile rat brain results in rapid biomechanical alterations: neurovascular mechanism as a putative confounding factor, J. Cereb. Blood Flow Metab 36 (2016) 954–964, 10.1177/0271678X15606923. [PubMed: 26661178]

[81]. Herthum H, Shahryari M, Tzschätzsch H, Schrank F, Warmuth C, Görner S, Hetzer S, Neubauer H, Pfeuffer J, Braun J, Sack I, Real-time multifrequency MR elastography of the human brain reveals rapid changes in viscoelasticity in response to the Valsalva maneuver, Front. Bioeng. Biotechnol 9 (2021). https://www.frontiersin.org/articles/10.3389/fbioe.2021.666456 (accessed November 19, 2023).

[82]. Doyle KP, Simon RP, Stenzel-Poore MP, Mechanisms of ischemic brain damage, Neuropharmacology 55 (2008) 310–318, 10.1016/j.neuropharm.2008.01.005. [PubMed: 18308346]

[83]. Krassner M, Kauffman J, Sowa A, Cialowicz K, Walsh S, Farrell K, Crary J, McKenzie A, Postmortem changes in brain cell structure: a review, Free Neuropathol. 4 (2023) 10, 10.17879/freeneuropathology-2023-4790.

[84]. Holland MA, Miller KE, Kuhl E, Emerging brain morphologies from axonal elongation, Ann. Biomed. Eng 43 (2015) 1640–1653, 10.1007/s10439-015-1312-9. [PubMed: 25824370]

[85]. Laughlin SB, Sejnowski TJ, Communication in neuronal networks, Science 301 (2003) 1870–1874, 10.1126/science.1089662. [PubMed: 14512617]

[86]. Berger C, Bauer M, Wittig H, Scheurer E, Lenz C, Post mortem brain temperature and its influence on quantitative MRI of the brain, Magn. Reson. Mater. Phys. Biol. Med 35 (2022) 375–387, 10.1007/s10334-021-00971-8.

[87]. Liu Y-L, Liu D, Xu L, Su C, Li G-Y, Qian L-X, Cao Y, In vivo and ex vivo elastic properties of brain tissues measured with ultrasound elastography, J. Mech. Behav. Biomed. Mater 83 (2018) 120–125, 10.1016/j.jmbbm.2018.04.017. [PubMed: 29702328]

[88]. Hou Z, Bayly PV, Okamoto RJ, Shear wave speeds in nearly-incompressible fibrous materials with two fiber families, J. Acoust. Soc. Am 149 (2021) 1097–1106, 10.1121/10.0003528. [PubMed: 33639778]

[89]. Jyoti D, McGarry M, Caban-Rivera DA, Van Houten E, Johnson CL, Paulsen K, Transversely-isotropic brain in vivo MR elastography with anisotropic damping, J. Mech. Behav. Biomed. Mater 141 (2023) 105744, 10.1016/j.jmbbm.2023.105744. [PubMed: 36893687]
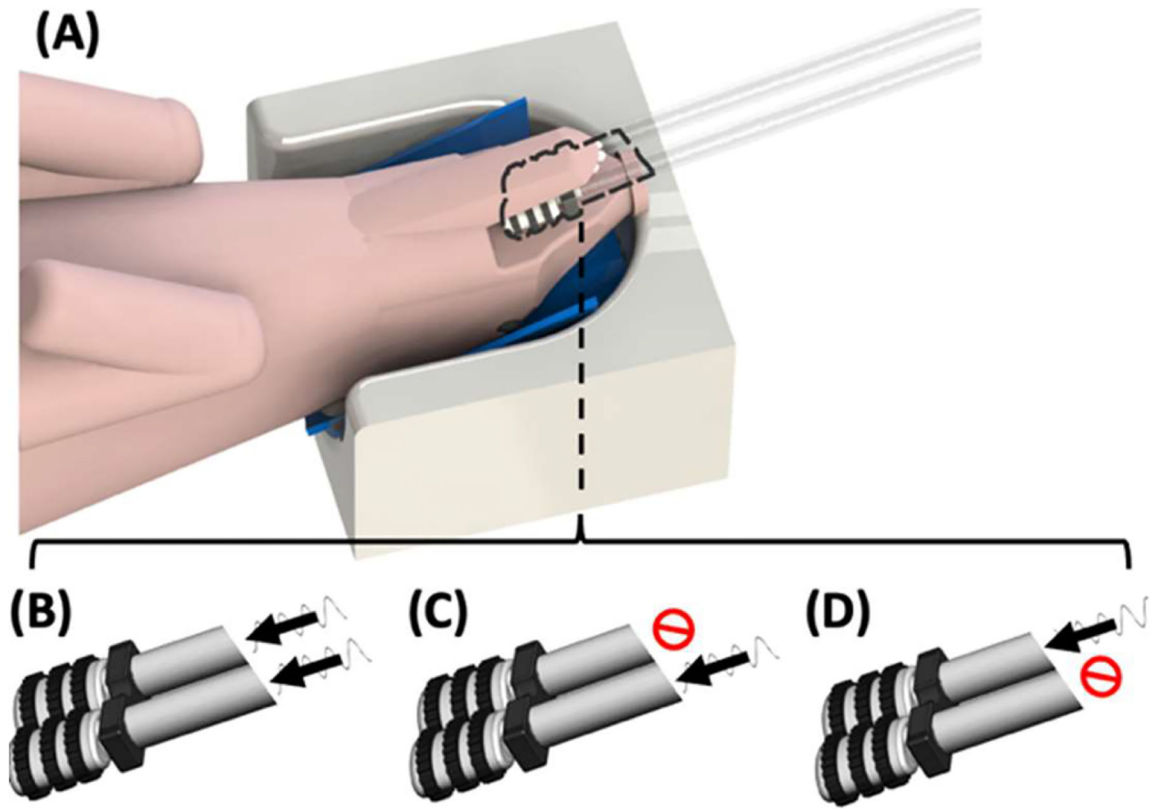
Fig. 1.
(A) Experimental set-up for MRE. Anesthetized minipig is placed in dorsal recumbency with its head placed in the lower part of the Siemens Head/Neck20 coil. Insets show the custom actuator, which is inserted into the mouth, preloaded against the molars, and driven by the Resoundant™ pneumatic driver. Three configurations are used to induce shear waves in brain at 100 Hz. (B) "Both" actuator configuration. (C) "Right" actuator configuration. (D) "Left" actuator configuration. Adapted from [32].
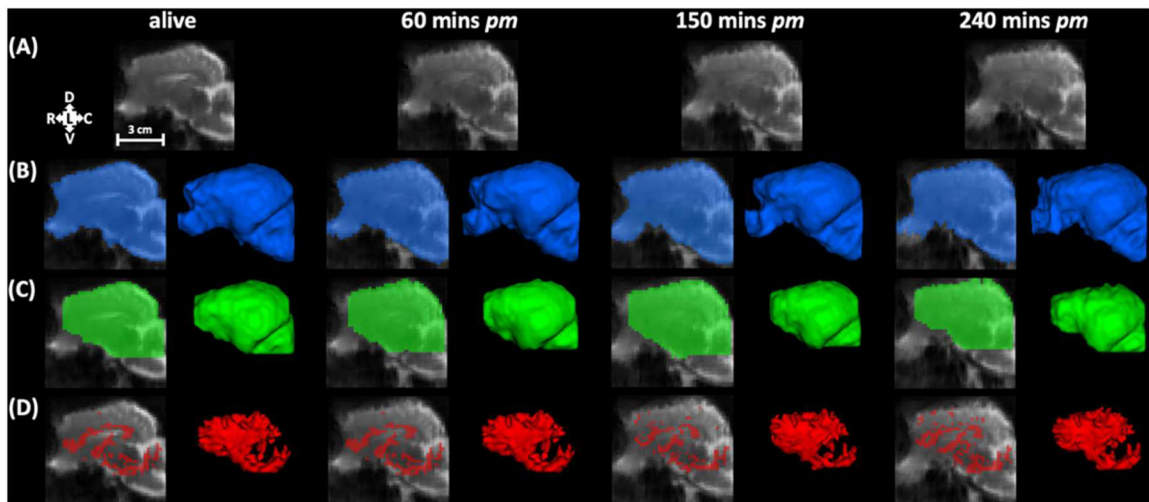
Fig. 2.
(A) Representative MRE magnitude image slice in the sagittal plane. (B) Brain volume of interest (VOI or "mask") used for MRE data processing in animal MP6. (C) Brain VOI without medulla, pons, and olfactory bulbs, used for TI-NLI in animal MP6. (D) White matter mask in animal MP6. Masks are depicted on the image slice (left) and as volume rendering (right) at each time point.
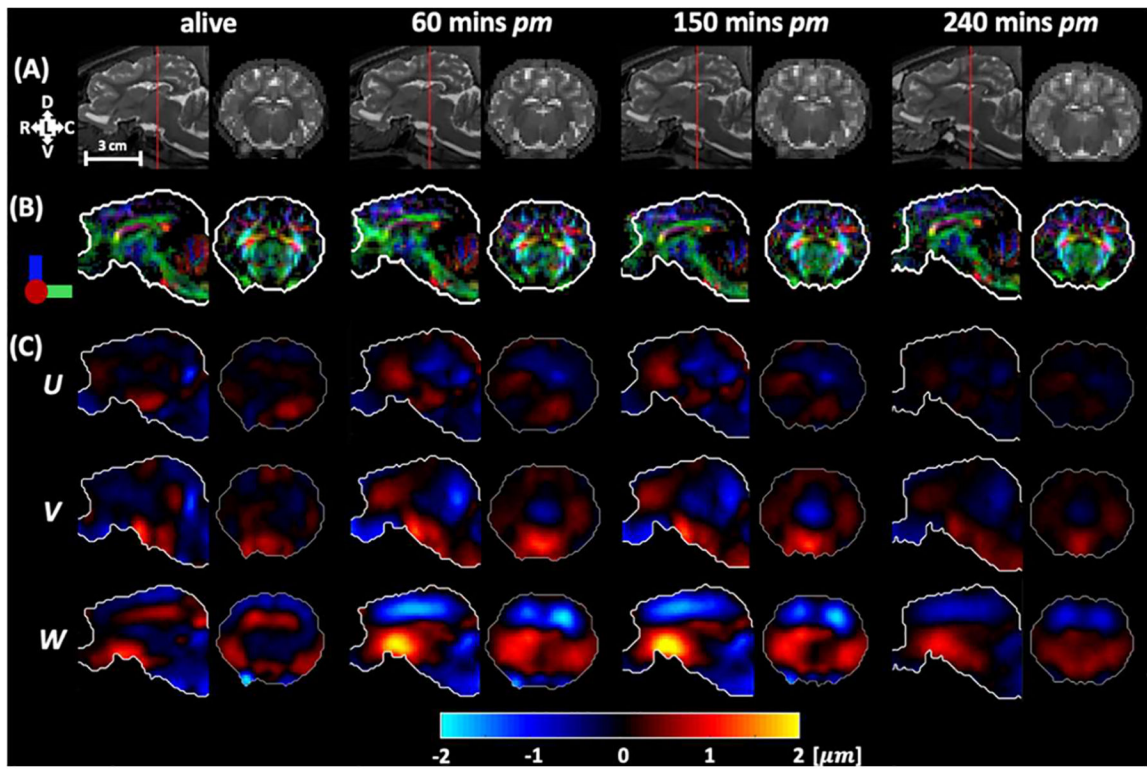
Fig. 3.
Example images of animal MP6. (A) T_2-weighted anatomical image slices in sagittal and axial planes. (B) Directionally encoded DTI color map where colors indicate the direction of maximum diffusivity (red = RL, green = RC, blue = DV) and brightness indicates diffusion anisotropy (FA). (C) MRE data acquired with the "Both" actuator configuration: *U, V,* and *W* wave displacement components corresponding to RL, DV, and RC motion, respectively. DV: dorsal-ventral; RC: rostralcaudal; RL: right-left.
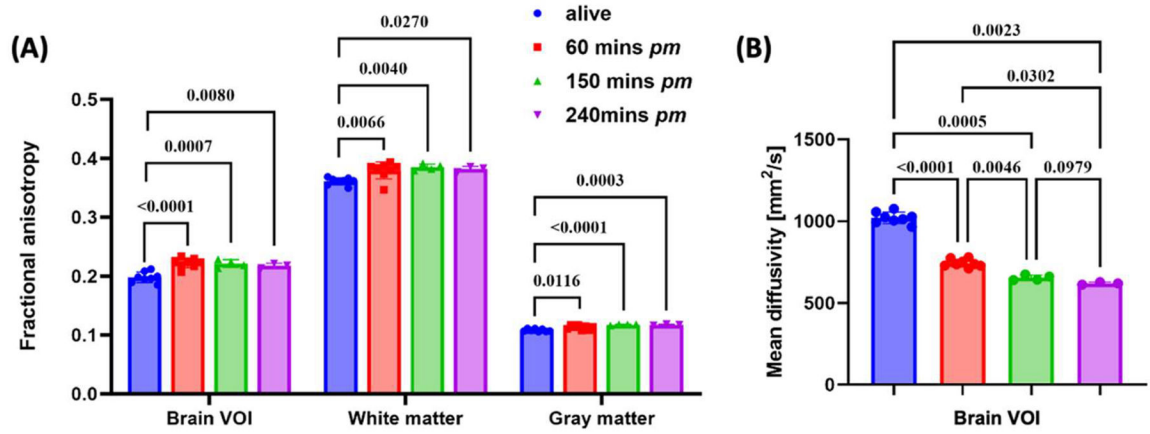
Fig. 4.

(A) Mean fractional anisotropy (FA) for all eight minipigs *in vivo* and post-mortem. (B) Mean values of mean diffusivity (MD) for all eight minipigs in brain volume of interest. Each marker represents the mean value for each individual minipig. Bars denote standard deviations. Note that data at 150 mins post-mortem were obtained only in four minipigs and data at 240 mins post-mortem were obtained only in three minipigs.
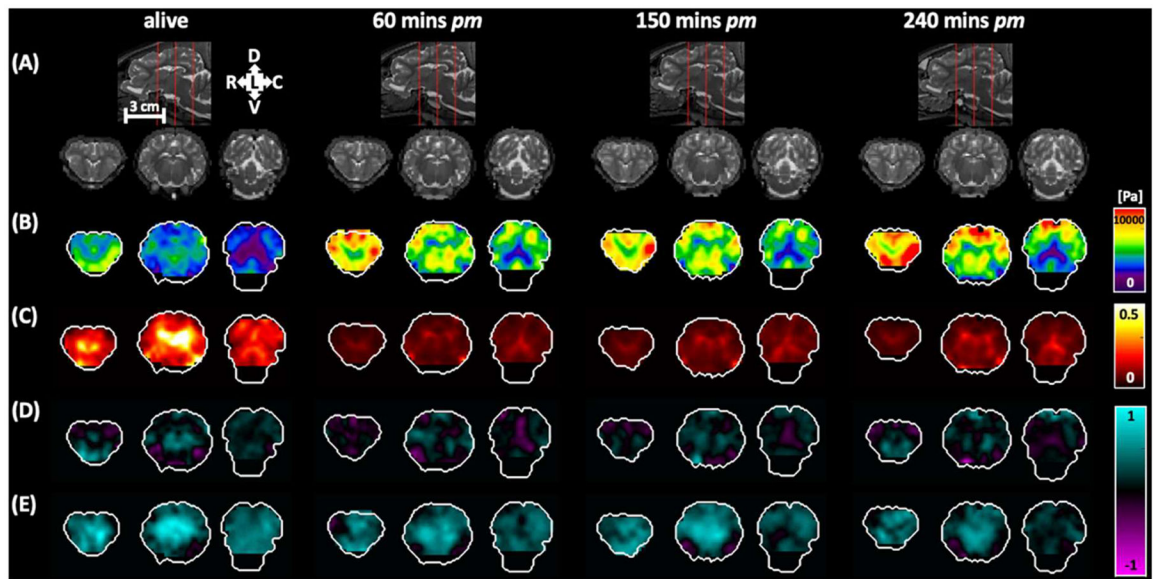
Fig. 5.
Maps of mechanical properties estimated by TI-NLI using all combinations of input data sets (actuator configurations) for three axial slices of the minipig brain in animal MP6. (A) T^2-weighted images in sagittal and coronal planes with coronal slice position shown in sagittal image. (B) Shear stiffness (μ). (C) Damping ratio (ξ). (D) Shear anisotropy (ϕ). (E) Tensile anisotropy (ζ).
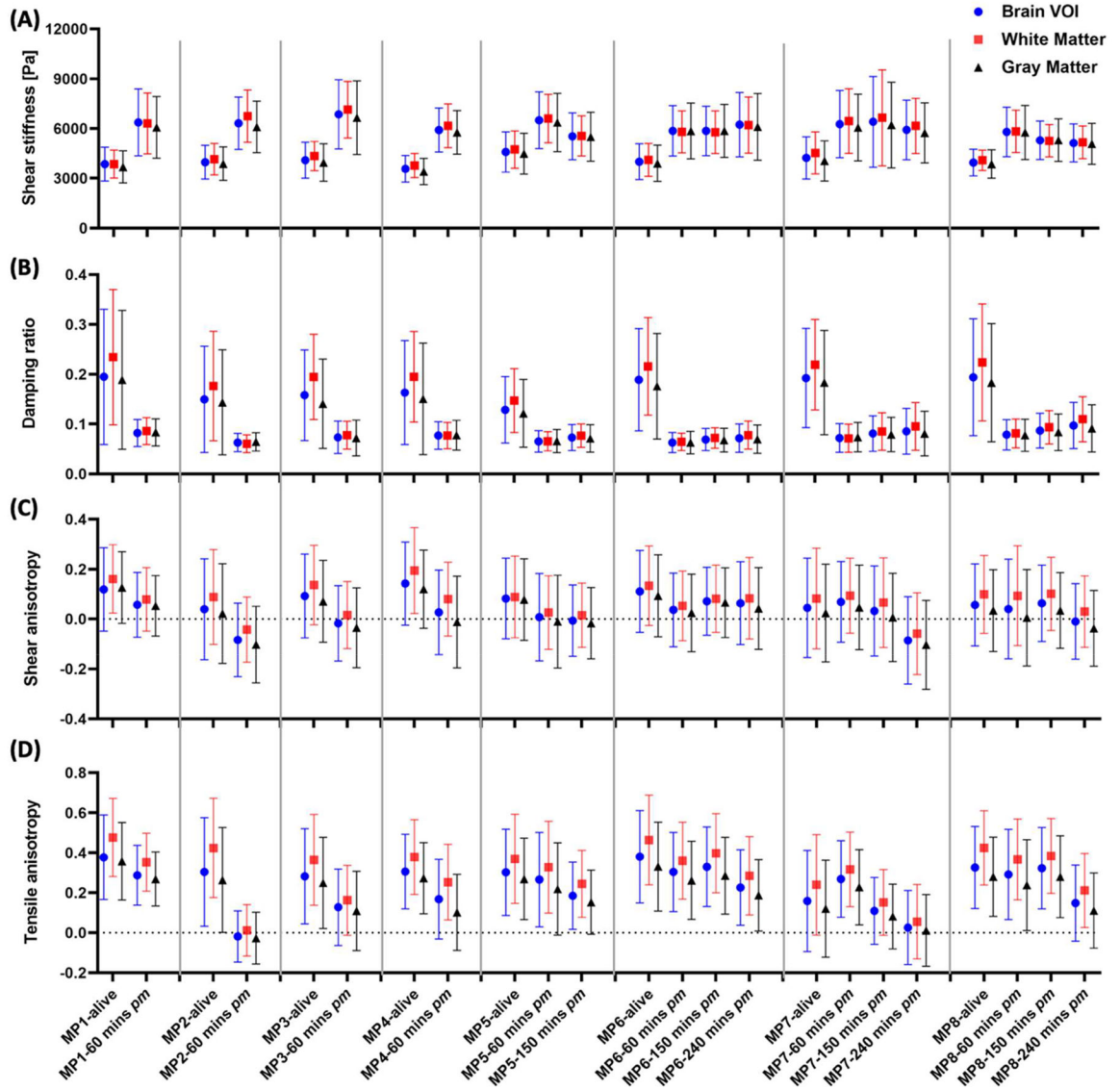
Fig. 6.
TI-NLI-estimated mechanical properties for each animal, at each scanning time, in the brain volume of interest, in WM, and in GM. (A) Shear stiffness (μ). (B) Damping ratio (ξ). (C) Shear anisotropy (ϕ). (D) Tensile anisotropy (ζ). Markers denote mean values; error bars denote ± 1 standard deviation.
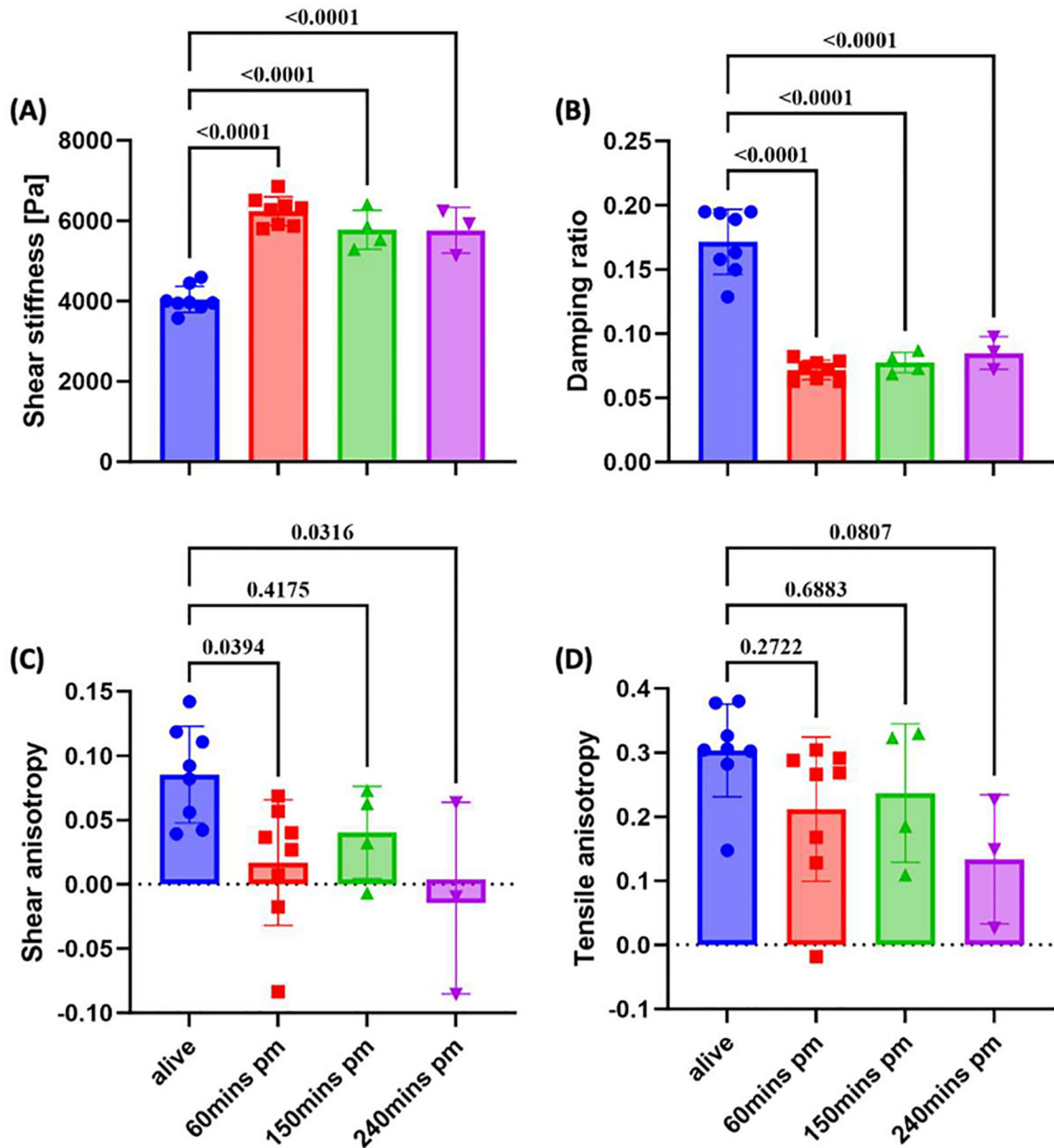
Fig. 7.
Mean TI-NLI-estimated mechanical properties within the brain volume of interest for all eight minipigs. Each marker represents the mean value for an individual minipig; error bars denote standard deviations. (A) Shear stiffness (μ). (B) Damping ratio (ξ). (C) Shear anisotropy (ϕ). (D) Tensile anisotropy (ζ). (Data at 150 mins post-mortem were obtained only in four minipigs and data at 240 mins post-mortem were obtained only in three minipigs.).
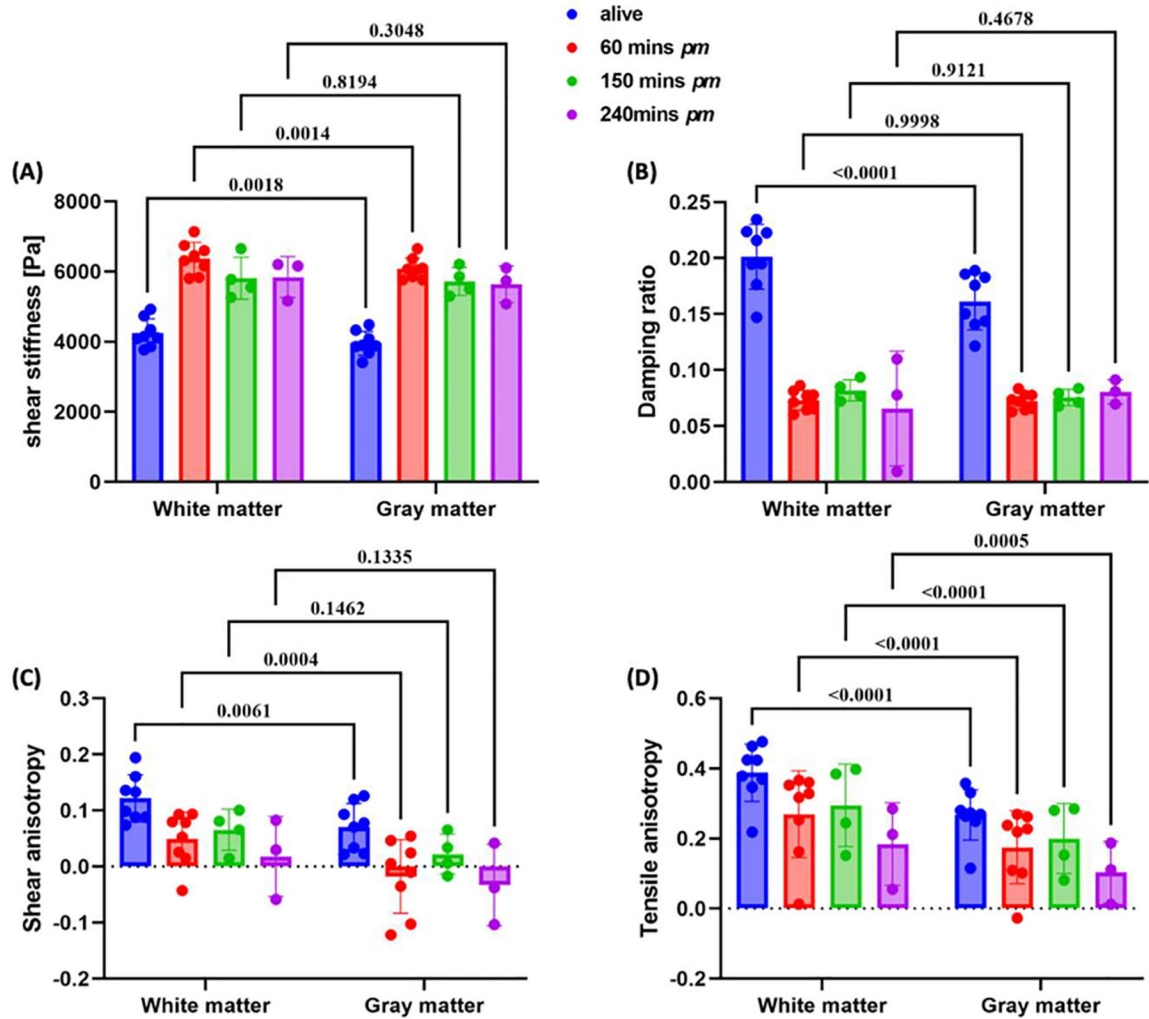
Fig. 8.
Mean TI-NLI-estimated mechanical properties of WM and GM for all eight minipigs. Each marker represents the mean value for an individual minipig; error bars denote standard deviations. (A) Shear stiffness (μ). (B) Damping ratio (ξ). (C) Shear anisotropy (ϕ). (D) Tensile anisotropy (ζ). (Measurements at 150 mins post-mortem were obtained only in four minipigs and measurements at 240 mins post-mortem were obtained only in three minipigs)